Journal of Asian Earth Sciences 202 (2020) 104535

Contents lists available at ScienceDirect

Journal of Asian Earth Sciences

journal homepage: www.elsevier.com/locate/jseaes

Crustal structure underneath central China across the Tibetan Plateau, the North China Craton, the South China Block and the Qinling-Dabie Orogen constrained by multifrequency receiver function and surface wave data

Zigen Wei[a], Zhiwei Li[b,*], Ling Chen[c,d,e], Risheng Chu[a], Shanshan Wu[f], Yuan Ling[g], Qiu Zeng[a]

[a] State Key Laboratory of Geodesy and Earth's Dynamics, Innovation Academy for Precision Measurement Science and Technology, Chinese Academy of Sciences, Wuhan 430077, China
[b] Science and Technology on Reliability and Environmental Engineering Laboratory, Beijing Institute of Spacecraft Environment Engineering, Beijing 100094, China
[c] State Key Laboratory of Lithospheric Evolution, Institute of Geology and Geophysics, Chinese Academy of Sciences, Beijing 100029, China
[d] University of Chinese Academy of Sciences, Beijing 100049, China
[e] CAS Center for Excellence in Tibetan Plateau Earth Sciences, Beijing 100101, China
[f] Shanghai Earthquake Agency, Shanghai 200062, China
[g] Key Laboratory of Earth and Planetary Physics, Chinese Academy of Sciences, Beijing 100029, China

ARTICLE INFO

Keywords:
Crustal structure
Craton and orogen
Lower crustal flow
Multi-frequency receiver function
Phase velocity dispersion curve

ABSTRACT

Investigating the crustal structure at the juncture region of the Tibetan Plateau, the North China Craton, the South China Block and the Qinling-Dabie Orogen is important to understand processes of uplift of the Tibetan Plateau and the craton destruction and preservation. In this study, we dropped the H-k stacking of receiver functions (RFs), RF nonlinear inversion, and joint inversion of RF and surface wave dispersion with multiple Gaussian factors successively to invert the crustal thickness (H), average Vp/Vs ratio (k) and S-wave velocity in the juncture region. The imaging results and the synthetic tests of multifrequency H-k stacking were further used to study the crustal structure and related tectonic evolution. Our results show that the H and k values generally increase and decrease, respectively, as the Gaussian factor increases in the study region, which is consistent with synthetic tests of H-k stacking. The cores of the Ordos Block and the Sichuan Basin exhibit a typical cratonic crust, whereas the Zhongtiao Mountains and adjacent Qinling-Dabie Orogen to the south may have undergone delamination of the lower crust. Local low-velocity anomalies in the middle-lower crust were observed in the Western Qinling Orogen and Qilian Orogen, whereas high S-wave velocities in the middle-lower crust were observed at the juncture region between the Western Qinling Orogen and the Qinling-Dabie Orogen. Our results suggest that the lower crustal flow is probably restricted to the central area in the Western Qinling Orogen and does not flow into the Qilian Orogen or the Qinling-Dabie Orogen.

1. Introduction

The juncture region of the Tibetan Plateau, the North China Craton, the South China Block and the Qinling-Dabie Orogen is located in a major transition zone between the E-W and N-S tectonic domains in mainland China (Fig. 1). Since the Cenozoic, the tectonic setting of this region has been impacted by the westward subduction of the Pacific Plate and the northward convergence of the Indian Plate with the Eurasian Plate (Ren et al., 2002; Deng et al., 2003; Wang et al., 2014). This special geographical location and tectonic environment make the region an ideal place for studying the uplift process and dynamics mechanism of the Tibetan Plateau, cratonic destruction and preservation, and the formation and reorganization of orogenic belts (Griffin et al., 1998; Yin and Harrison, 2000; Tapponnier, 2001).

Some valuable results have been obtained in the study region by numerous geological and geophysical studies in recent years. Lower crustal flow has been proposed to be occurring in the central Tibetan Plateau and is considered an important uplift mechanism of the Tibetan Plateau (Clark and Royden, 2000). A thick lithosphere and cratonic crust have been imaged in the Ordos Block and the Sichuan Basin, and these regions are believed to have maintained structural stability for a long time (Chen et al., 2009; Zheng et al., 2009; Zhao et al., 2013). However, there are still some controversial issues, such as the extension direction and range of the lower crustal flow (Pan and Niu, 2011; Shen

* Corresponding author.
E-mail address: zwli@whigg.ac.cn (Z. Li).

https://doi.org/10.1016/j.jseaes.2020.104535
Received 18 September 2019; Received in revised form 20 August 2020; Accepted 20 August 2020
Available online 01 September 2020
1367-9120/ © 2020 Elsevier Ltd. All rights reserved.

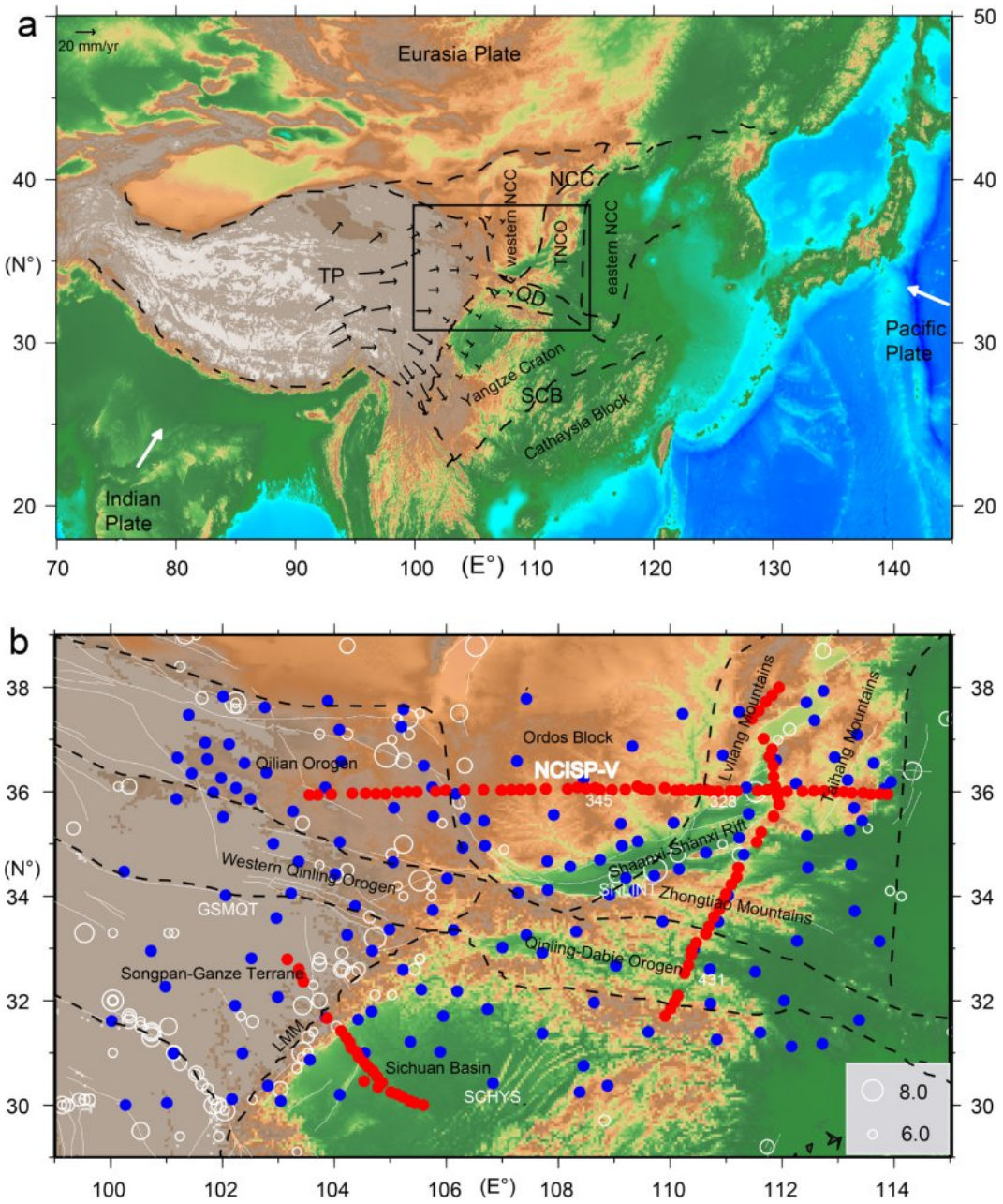

Fig. 1. Topography, tectonic setting and seismic station distribution in the study region. White arrows (a) show the westward subduction and northward convergence of the Pacific Plate and the Indian Plate to the Eurasian Plate, respectively. Black arrows indicate the observed GPS velocity field in the study region relative to the stable Eurasia Plate (Gan et al., 2007). Red and blue solid dots (b) mark the locations of temporary and permanent seismic stations, respectively. Black dashed lines and white circles show the tectonic boundaries (Zhao et al., 2005) and the > 6.0 magnitude earthquakes that occurred from 1500 CE to 2018 (China Earthquake Networks Center), respectively. White lines show the active faults (Deng et al., 2003). TP: Tibetan Plateau; NCC: North China Craton; SCB: South China Block; TNCO: Trans-North China Orogen; QD: Qinling-Dabie Orogen. (For interpretation of the references to color in this figure legend, the reader is referred to the web version of this article.)

et al., 2015), and the dynamic mechanism of uneven lithospheric modification in the Trans-North China Orogen (Zhao et al., 2013; Jiang et al., 2013). Therefore, it is necessary to conduct more research on deep structures in this region from different perspectives and using different methods.

The velocity, thickness and Vp/Vs ratio are closely related to the rock composition and stress state of the crust, and these parameters can provide constraints on regional crustal structural characteristics and continental tectonic evolution (Christensen, 1996; Ji et al., 2009). The joint inversion of receiver function (RF) and surface wave dispersion can reduce the nonuniqueness and increase the resolution of the inversions associated with each individual data set (Julià et al., 2000). This technique has been commonly applied to invert for the crust-mantle velocity structure in recent years (Hu et al., 2005; Liu et al., 2014; Deng et al., 2018). Based on teleseismic waveform data from three dense temporary arrays and relatively evenly distributed permanent stations and collected phase velocity dispersion curves with periods of 5–60 s (Shen et al., 2016; Ling et al., 2017), we used the multifrequency H-k stacking of RFs, multifrequency RF nonlinear inversion, and joint inversion of multifrequency RF and surface wave dispersion to image the crustal thickness, Vp/Vs ratio and S-wave velocity at the juncture region among the Tibetan Plateau, the North China Craton, the South China Block and the Qinling-Dabie Orogen. Based on the imaging results and the theoretical analysis of the multifrequency H-k stacking

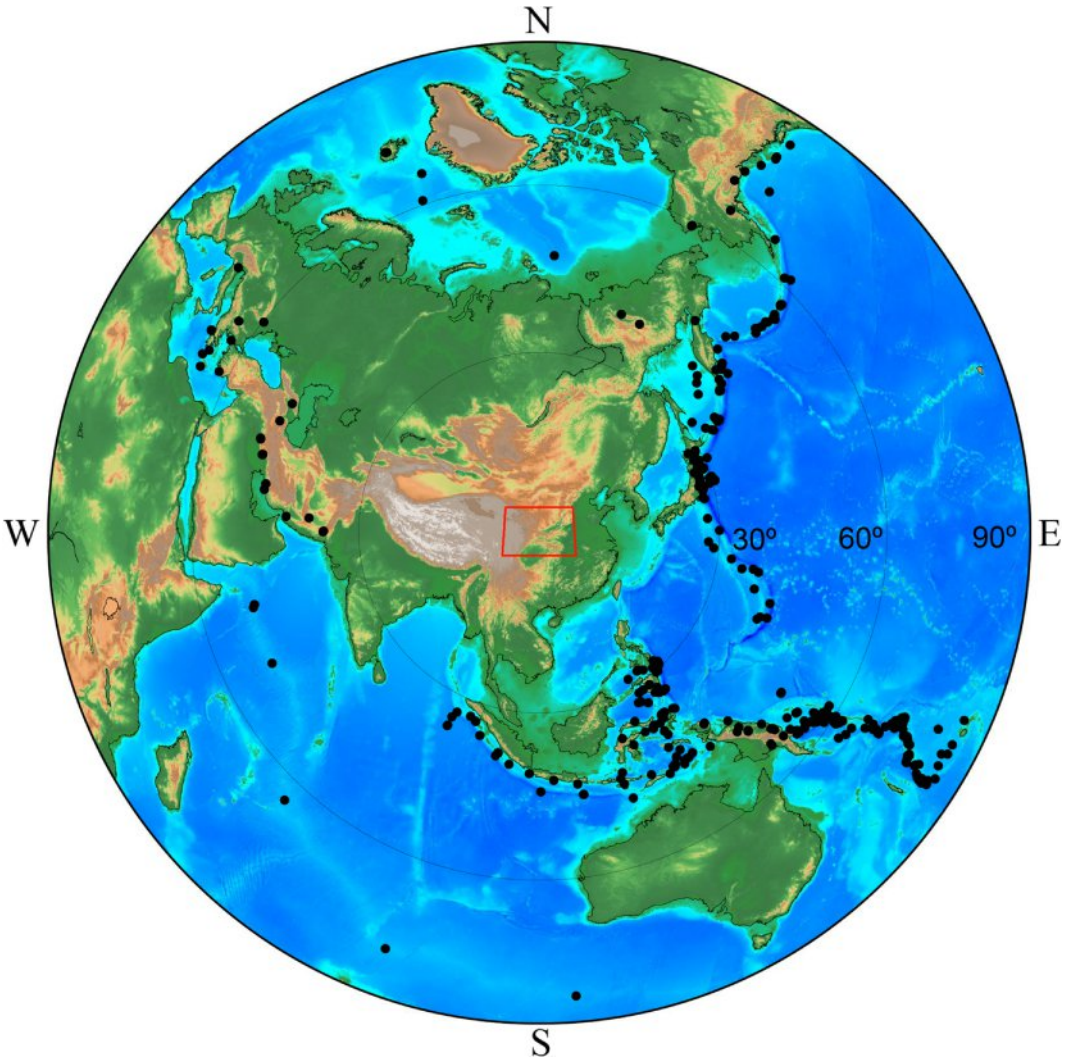

Fig. 2. Teleseismic event distribution (black solid dots) used in the study. The red quadrangle shows the study region. (For interpretation of the references to color in this figure legend, the reader is referred to the web version of this article.)

of RFs, we further studied the crustal structure and related tectonic evolution of the study region.

2. Geological setting

The North China Craton is composed of eastern and western Archean continental blocks sutured along the central Trans-North China Orogen before ~1.85 Ga (Zhao et al., 2005). The South China Block, containing > 2.0 Ga crustal rocks, was formed through the amalgamation between the Cathaysia Block and the Yangtze Craton along the Sibao orogen at ca.880 Ma or soon after (Li et al., 2009). During the Triassic, the North China Craton collided with the South China Block along the Qinling-Dabie Orogen, exposing ultrahigh-pressure eclogite and gneiss (Li et al., 1993). The Tibetan Plateau, experiencing stepwise rise and growth, has formed through the amalgamation of multiple microplates since 55 Ma (Tapponnier, 2001) and collided with the structural unit comprising the North China Craton, the South China Block and the Qinling-Dabie Orogen. The tectonic setting, which is influenced by both Pacific Plate subduction and the India-Eurasia collision, has produced numerous large-scale active faults and moderate-strong earthquakes in the study region (Ren et al., 2002; Deng et al., 2003; Wang et al., 2014; Yan et al., 2018).

Increasing numbers of geological and geophysical studies indicate lithospheric modification and lateral heterogeneity in our study region. A normal crustal thickness of ~38–45 km and an average P-wave crustal velocity of ~6.35 km/s (Zhang et al., 2003; Li et al., 2006; Liu et al., 2014; Wang et al., 2014) and a lithospheric thickness > 200 km (Chen et al., 2009; Zhao et al., 2013) have been observed in the Ordos Block and in the Sichuan Basin, indicating long-term survival of the lithospheric fabrics in these regions. Crustal thicknesses of 30–45 km (He et al., 2014; Wei et al., 2016; Wang et al., 2017), lithospheric thicknesses of 60–130 km (Chen et al., 2009; Jiang et al., 2013) and relatively low S-wave velocities in the upper mantle have been imaged in the Trans-North China Orogen, and crustal and lithospheric modification and thinning are through to have occurred in this region. Lateral variations in crustal and lithospheric thickness have been imaged in the northeastern Tibetan Plateau (Pan and Niu, 2011; Shen et al., 2016; Wang et al., 2017) and are related to its formation and tectonic evolution history. Significant low-velocity material has been observed in the middle and lower crust of the central and eastern Tibetan Plateau (Bao et al., 2013;Li et al., 2014; Shen et al., 2015). These low velocities are possibly associated with lower crustal flow, which is considered one of the uplift mechanisms of the Tibetan Plateau, and this inference is supported by magnetotelluric observations (e.g., Bai et al., 2010) and GPS data (e.g., Gan et al., 2007). Striking E-W differences in crustal and lithospheric thicknesses have also been imaged in the Qinling-Dabie Orogen (Zheng et al., 2010a, 2010b; Jiang et al., 2013; Wei e al., 2016), and these differences are mainly related to different

tectonic settings between the eastern and western parts (Ren et al., 2002; Deng et al., 2003; Wei et al., 2016).

3. Data and method

3.1. Data

Receiver functions from teleseismic waveforms and phase velocity dispersion curves of Rayleigh waves were used to invert for the crustal structure in this study. The teleseismic data are derived from two different sources (Fig. 1). The two-year data from 146 permanent broadband seismic stations were obtained from the Data Management Center of China National Seismic Network, Waveform data of China National Seismic Network, Institute of Geophysics, China Earthquake Administration (doi: 10.11998/SeisDmc/SN, htTibetan Plateau:// www.seisdmc.ac.cn, Zheng et al., 2010a, 2010b). The data from 109 temporary broadband seismic stations, which had an average spacing of 10–20 km and were operated for 12–18 months, were obtained from the Seismic Array Laboratory, Institute of Geology and Geophysics, Chinese Academy of Sciences. These data on earthquakes with epicentral distances ranging from 30° to 90° and > 5.5 magnitudes (Fig. 2) were used to estimate the radial RFs using the time-domain iterative deconvolution method (Herrmann, 2013). The RFs with unclear P-waves or indistinguishable Ps arrivals were removed by visual inspection. Waveforms with correlation coefficients of < 0.9 between stacked waveforms from all RFs and individual waveforms were further deleted.

Phase velocity dispersion curves at different stations were constructed from the different results. For profile NCISP-V (Fig. 1, Fig. 3a), curves of 5–20 s, 31–60 s and 21–30 s periods were calculated by ambient noise tomography (Ling et al., 2017), surface wave tomography (Wei et al., 2015) and their average, respectively. For other stations, the phase velocity dispersion data for periods from 8 s to 50 s periods were from the new crust-mantle seismic reference model beneath China, based on surface wave dispersion with a lateral resolution of 0.5° (Shen et al., 2016).

3.2. Methods

3.2.1. Multifrequency H-k stacking method of receiver functions

The arrival times of different phases from the Moho are usually used to study the crustal structure. The H-k stacking method of RFs (Zhu and Kanamori, 2000) integrates the time differences between the incident P-wave and the three phases of the Moho (converted Ps and multiple PpPs and PpSs + PsPs phases) to estimate crustal thickness (H) and average Vp/Vs ratio (k) under each station. In an assumed 1D single-layer crustal model, the maximum stacking amplitude corresponds to the best H and k. In this study, we used different Gaussian factors of 1.0, 2.0 and 3.0, which balance the trade-off well between resolution preservation and suppression of high-frequency, to estimate H and k and used their average as the last result. We chose 6.35 km/s as the average crustal P-wave velocity according to seismic exploration data (Li et al., 2006), and different weights of 0.6, 0.3 and 0.1 for Ps, PpPs and PpSs + PsPs phases due to their progressive decrease in the signal-to-noise ratio. The stacked RF sets with 4° steps in each 8° epicentral distance range for all azimuths, and H-k stacking results are shown beneath typical stations in different tectonic units in Fig. 4. The consistency between the highest amplitudes and theoretical arrival times for three phases of the Moho and the small uncertainties of H-k stacking results suggest the reliability of the estimated H and k values.

3.2.2. Multifrequency receiver function nonlinear inversion method

The waveform inversion method, involving fitting a synthetic RF with the observed data, is widely used to image crustal S-wave velocities. Li et al. (2017) developed a multifrequency RF nonlinear inversion method based on the global optimizing algorithm of differential evolution. In this method, RFs with different frequency bands are used to simultaneously constrain both the long and short wavelength characteristics of the crustal velocity structures. In this study, we used this method to invert for the crustal S-wave velocities under each station using different Gaussian factors of 1.0, 2.0 and 3.0, which can distinguish a thin layer of ~1.5 km thick assuming average crustal S-wave velocity of 3.6 km/s. In the inversion, the initial crustal thickness and

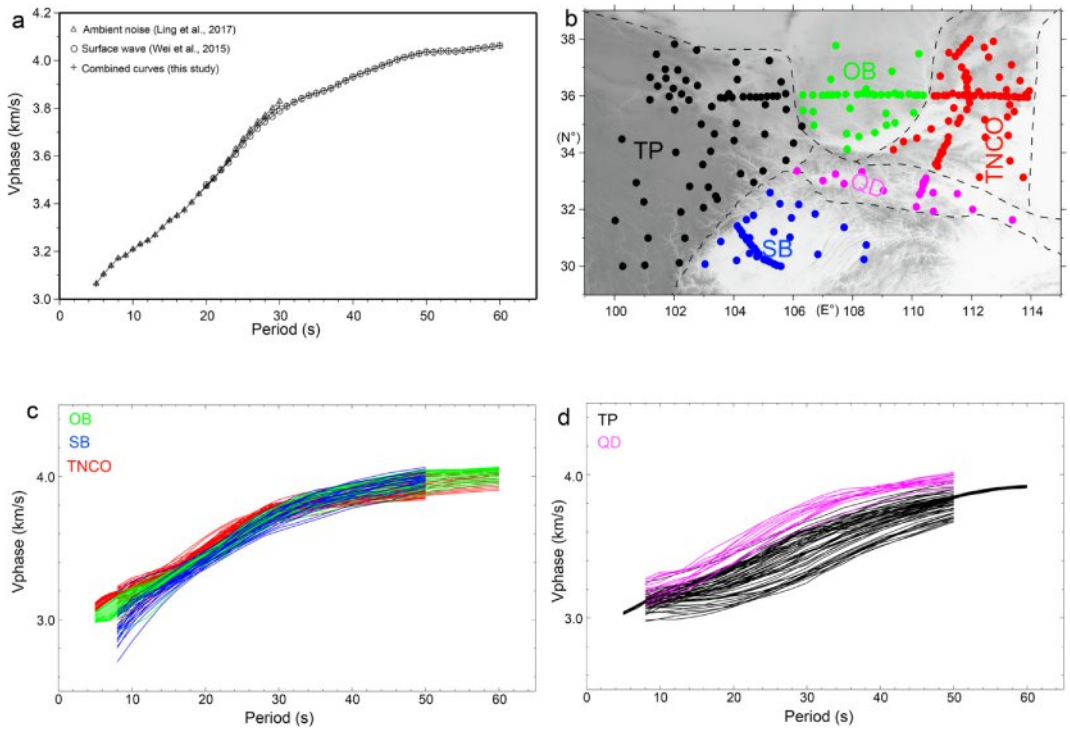

Fig. 3. Combined phase velocity dispersion curves for station 328 (a) and dispersion curves for different tectonic units marked by different colors (b, c, d). OB: Ordos Block; SB: Sichuan Basin; TNCO: Trans-North China Orogen; TP: Tibetan Plateau; QD: Qinling-Dabie Orogen.

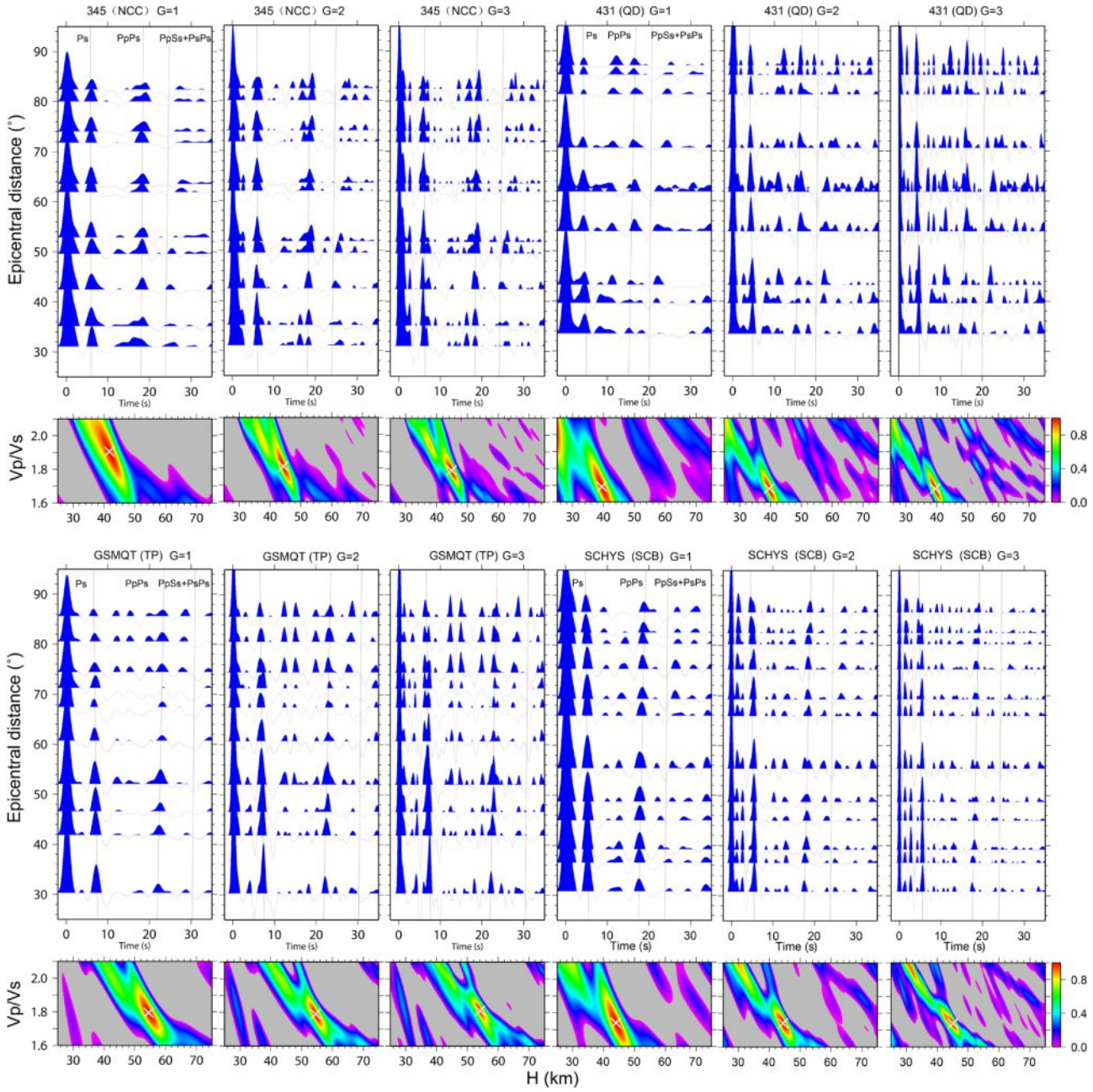

Fig. 4. H-k stacking results for typical stations in different Gaussian factors (G). Station locations are shown in Fig. 1. NCC: North China Craton; QD: Qinling-Dabie Orogen; TP: Tibetan Plateau; SCB: South China Block.

Vp/Vs ratio for each layer (given five-layer crust) for each station were based on the above H-k stacking results for the RFs. The CRUST 1.0 model (Laske et al., 2013) was also used to constrain the initial Vp and thickness for each layer. The crustal thickness and Vp for each layer vary by ± 2 km and ± 20%, respectively. The Vp/Vs ratio from the top layer to the bottom layer was set to k, 1.7, 1.73, 1.76 and 1.79 for k values of ≤ 1.76 and to k, 1.7, 1.74, 1.78 and 1.82 for k values of > 1.76. The Vp/Vs ratios in the top layer and in the other layers vary by ± 1 and ± 0.1, respectively. For stations with H values of ≤ 45 km, the fitting time window was set to 25 s after the P phase arrival, and the thickness for each layer varies by ± 5 km. For stations with H values of 45–55 km and ≥ 55 km, the fitting time window was set to 30 s after the P phase arrival, and the thickness for each layer varies by ± 8 km and ± 10 km, respectively. For the typical station 345, the recovered RFs at different frequencies all fit the real data well, particularly the Moho Ps and PpSs phases (Fig. 5a). The objective function decreases rapidly with the iteration increases (Fig. 5b). The well fit between the recovered RFs and real data and fast convergence of objective function suggest the reliability of the inverted S-wave velocity (Fig. 5c).

3.2.3. Joint inversion of multifrequency receiver function and surface wave dispersion

We used the joint inversion method of RF and surface wave dispersion (Herrmann, 2013) to invert for the S-wave velocity in the study region. In the inversion, the RFs with different Gaussian factors of 1.0, 2.0 and 3.0 and phase velocity dispersion curves were fitted simultaneously. The initial models of 2 km for each layer are from the smoothed results of the multifrequency RF nonlinear inversion method. The weighting factors for the RF and the surface wave dispersion curves were set to 0.5 and 0.5, respectively, for stations in the NCISP-V profile due to 0.1° lateral resolution, and to 0.7 and 0.3, respectively, for other

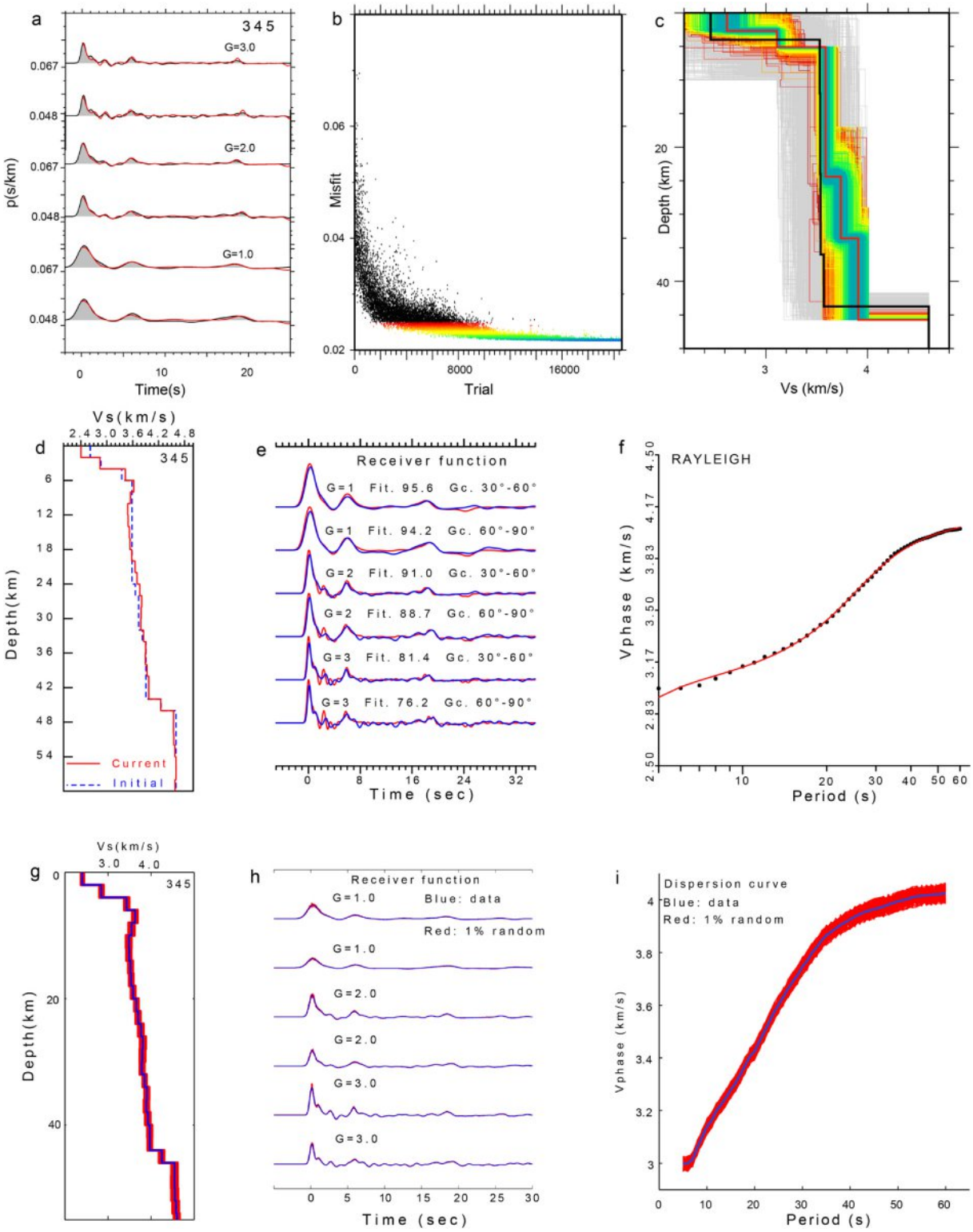

Fig. 5. Schematic diagrams for multifrequency receiver function nonlinear inversion (a, b, c) and joint inversion of multifrequency receiver function and surface wave dispersion (d, e, f) and effect of data uncertainty on inversion results (g, h, i). Red lines denote the recovered receiver functions (a, e), S-wave velocity models (c, d) and dispersion curve (f). Panel b shows that the objective function decreases with increasing iteration. In g, h, i, red lines show inverted S-wave velocity models (g) for 100 random RFs (h) and 100 random dispersion curves (i) within the ± 1% deviations of the observed data (blue line in h), respectively. G, Fit. and Gc. (a, e, h) represent the Gaussian factor, fitness and epicentral distance, respectively. (For interpretation of the references to color in this figure legend, the reader is referred to the web version of this article.)

stations because of the 0.5° lateral resolution of the surface wave dispersion (Shen et al., 2016). For stations with H values of ≤ 45 km, the fitting time window was set to −5–35 s, and the inversion depth was set to 60 km. For stations with H of > 45 km, the fitting time window was set to −5–40 s, and the inversion depth was set to 80 km. The RFs with fits of < 65% were removed to ensure the reliability of the

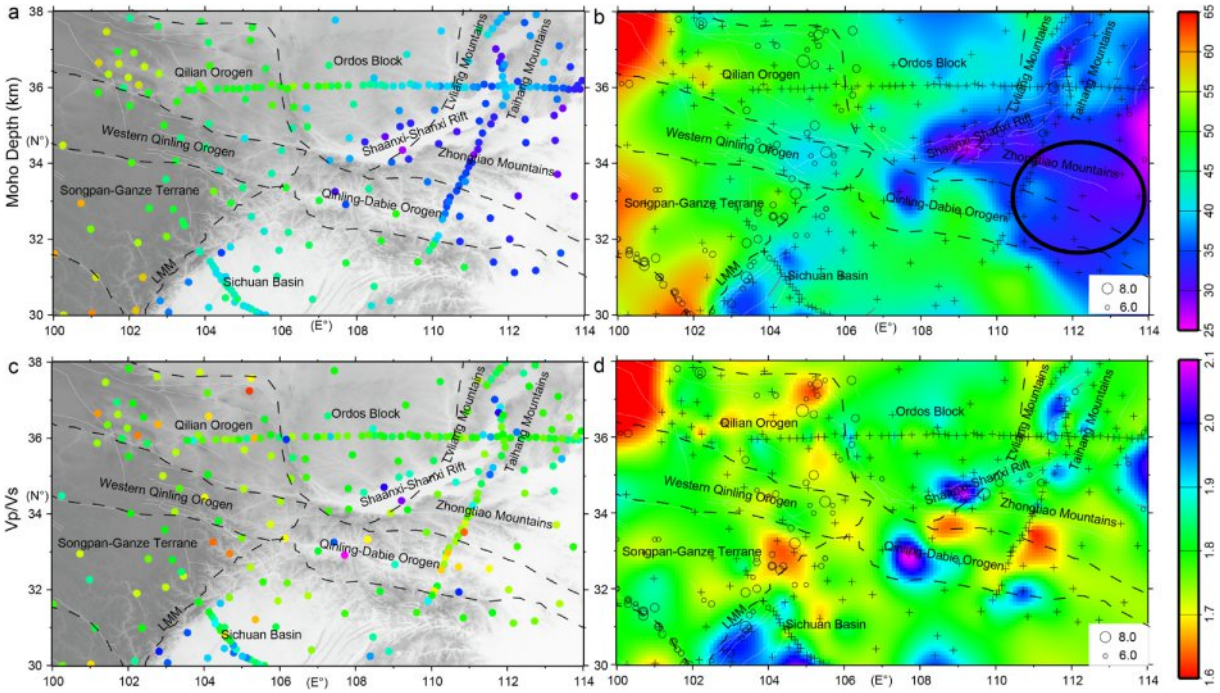

Fig. 6. Average Moho depth (a,b) and Vp/Vs ratio (c,d) for individual data points (a,c) and interpolated using the Generic Mapping Tools surface command (b,d) for the different Gaussian factors of 1.0, 2.0 and 3.0 in the study region. Color solid dots (a,c) and black crosses (b,d) mark the locations of seismic stations. Black dashed lines and black circles show the tectonic boundaries and the > 6.0 magnitude earthquakes that occurred from 1500 CE to 2018 (China Earthquake Networks Center), respectively. White lines show the active faults (Deng et al., 2003). Black ellipse in b marks the region where may have undergone delamination of the lower crust. LMM: Longmen Mountains.

inverted results. Fig. 5d,e,f shows the joint inversion results for a typical station. The recovered RFs in different frequency and phase velocity dispersion curves all fit the real data well, suggesting the reliability of the inverted S-wave velocity data. 100 inversion runs were further performed using different data sets for random RFs (Fig. 5h) and random dispersion curves (Fig. 5i) within the ± 1% deviations of the observed data, respectively, to analyze the effects of data uncertainty. The S-wave velocities (Fig. 5g) from the 100 random inversions and the corresponding final inverted model show small variations and have similar patterns of velocity variation with depth, suggesting the stability and reliability of the joint inversion results.

4. Results

4.1. Moho depth and Vp/Vs ratio

The average Moho depth and Vp/Vs ratio from H-k stacking of RFs are shown in Fig. 6 for different Gaussian factors of 1.0, 2.0 and 3.0. The Moho depth roughly thickens westward from ~26 to ~64 km (Fig. 6a,b) and shows strong lateral inhomogeneity. The Vp/Vs ratio (Fig. 6c,d) exhibits complex variations, with high (> 1.87) and low (< 1.73) anomalies in local areas. The Moho depth and Vp/Vs ratio are generally < 40 km and 1.76, respectively, in the Zhongtiao Mountains (Trans-North China Orogen) and Qinling-Dabie Orogen to the south and change slightly to approximately 40 km and 1.78, respectively, in the core of the Ordos Block. In some areas of the Shaanxi-Shanxi Rift, the Moho depth is generally < 35 km, and the Vp/Vs ratio is > 1.87. In the Qinling-Dabie Orogen, the Moho depth is generally < 40 km in the eastern part but > 40 km in the western part, and the Vp/Vs ratio varies mainly from 1.7 to 2.0. In the Yangtze Craton, the Moho depth is generally thicker than 45 km, and the Vp/Vs ratio is approximately 1.78 in the northern part. The Moho depth varies from 40 to 45 km in the Sichuan Basin, and the Vp/Vs ratio exhibits generally high anomalies of > 1.87 beneath the Longmen Mountains. In the northeastern Tibetan Plateau, the Modo depth is generally thicker than 45 km and thickens to the west, and the Vp/Vs ratio is mainly within the range of 1.7–1.8. Earthquakes with magnitudes > 6.0 mainly occurred in areas with significant lateral variations in the Moho depth and Vp/Vs ratio, such as rift zones and the boundary between the Yangtze Craton and the Tibetan Plateau. These areas usually contain many faults and have heterogeneous crustal compositions, which can readily accumulate energy and trigger earthquakes.

4.2. Crustal S-wave velocity structure

Fig. 7 shows the S-wave velocity distribution at different depths by the joint inversion of the multifrequency RF and surface wave dispersion. Significant differences in the S-wave velocity were imaged among different blocks. At a depth of 2 km, an obvious low velocity of < 2.8 km/s was found in the Ordos Block and Sichuan Basin, and a relatively high velocity of > 3.0 km/s was imaged in most of the Qinling-Dabie Orogen and the Tibetan Plateau. At a depth of 10 km, the S-wave velocity is obviously lower in the Sichuan Basin and Shaanxi-Shanxi Rift than in other regions. At depths of 30 km and 38 km, the S-wave velocity shows an overall and significant low anomaly in the Songpan-Ganze Terrane. At depths from 10 km to 38 km, the S-wave velocity is relatively higher at the juncture region between the Western Qinling Orogen and the Qinling-Dabie Orogen than in the eastern and western areas. At depths from 10 km to 46 km, the S-wave velocity data show a local low-velocity anomaly in the Qilian Orogen and Western Qinling Orogen.

5. Discussion

Similarities, differences and lateral variations in the S-wave velocity, Moho depth and k were observed among different blocks in our study (Figs. 6 and 7), which are consistent with previous results using RF imaging (He et al., 2014; Tian and Zhang, 2013; Ye et al., 2017;

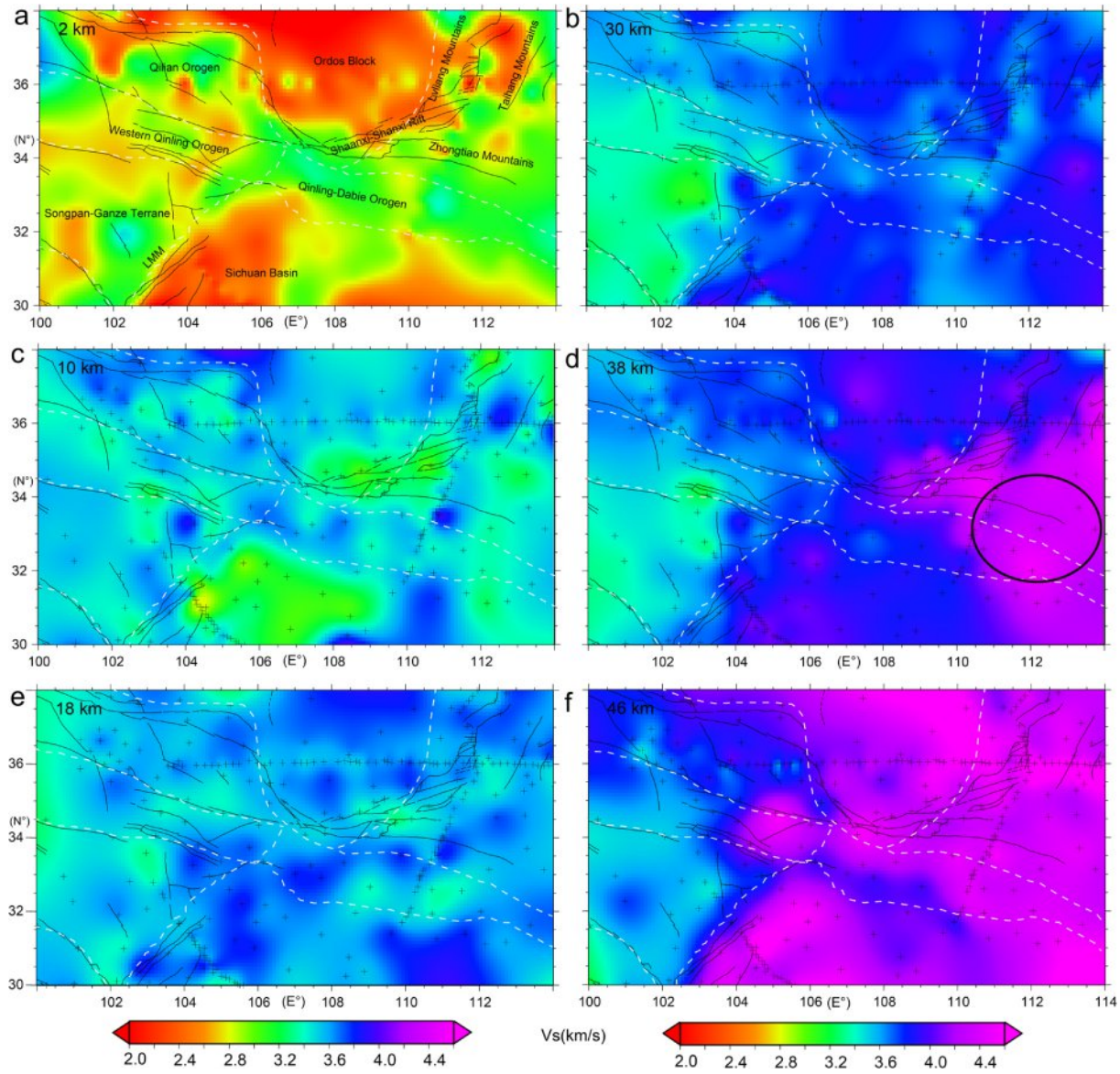

Fig. 7. The S-wave velocity distribution at different depths in the study region. Black ellipse in d marks the region where may have undergone delamination of the lower crust. LMM: Longmen Mountains.

Wang et al., 2017), surface wave tomography (Zheng et al., 2010a, 2010b; Bao et al., 2013; Jiang et al., 2013), seismic exploration (Li et al., 2006), magnetotelluric sounding (Bai et al., 2010; Zhang et al., 2012) and other methods. In addition, a more detailed crustal structure in some areas was revealed in this study, which will be discussed by combining the S-wave velocity beneath five typical linear profiles and synthetic analysis of the H-k stacking methods.

5.1. Variation in H-k results with frequency in response to the sedimentary and crust-mantle transition structure in the study region

Complex and long-term tectonic evolution and extensive marine and continental sedimentation (Ren et al., 2002; Deng et al., 2003; Zhao et al., 2005) in the study region have inevitably influenced the structure of the shallow deposits and the crust-mantle transition zone (CMT). Synthetic H-k stacking tests for crustal models with different sediments and CMT structures were performed and were used to study the frequency response of the H-k results and to further analyze the sediments and CMT in the study region. A reflectivity technique (Levin and Park, 1997) was used to generate synthetic RFs with different Gaussian factors of 1.0, 2.0 and 3.0. The synthetic tests show (Figs. 8, 9, Table 1) that the phases from the sediment and CMT will interfere with the phases from the Moho to some degree, which leads to differences between the H-k results and the real values. The estimated crustal thickness from H-k stacking is close to the upper end of the estimated range in models with a gradual CMT, and the interface with the highest wave impedance in models with a zip CMT. The estimated H and k values are thinner and higher than the real values, respectively, except for the model containing only a single 6-km-thick layer of sediment. In models containing sediment and a CMT, the values of (k3-k1) (in Hi and ki, i represents the Gaussian factor) are negative; in models containing only the sediment, the values of (H3-H1) and (H3-H2) are positive, and the values of (k3-k2) are negative; and in models containing sediment and a zip CMT, the values of (k3-k2) are almost negative.

The difference in the H-k results with different Gaussian factors was further calculated in the study region to analyze the area's sedimentary and CMT structure (Fig. 10). The results generally show features similar to those of the synthetic tests. The values of (H3-H1)/H3 and (H3-H2)/H3 are generally positive and vary mainly by ± 10% and ± 5%, respectively. The values of (k3-k1)/k3 and (k3-k2)/k3 are generally

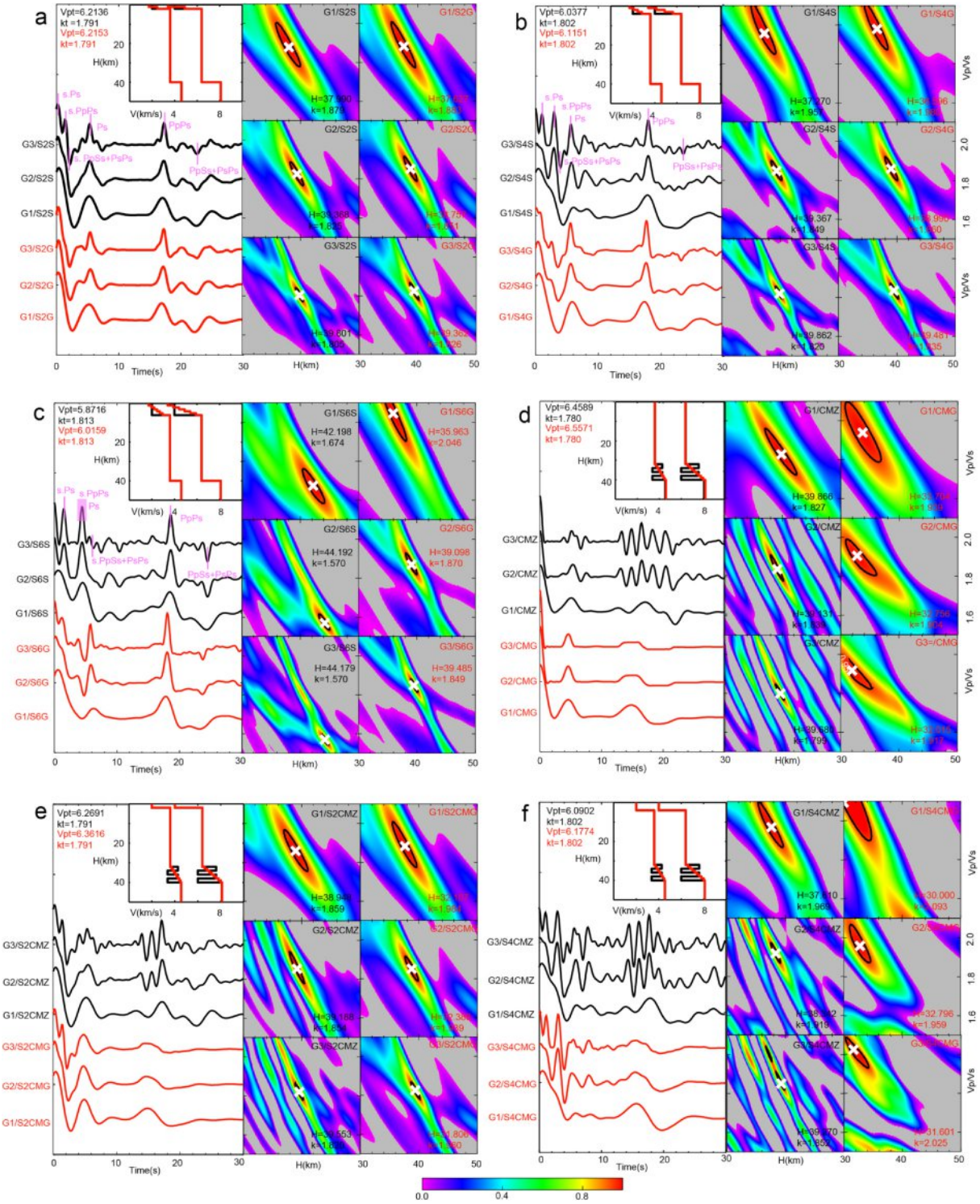

Fig. 8. Synthetic receiver functions and H-k stacking results for crustal models with different sediment and crust-mantle structures with Gaussian factors (G) of 1.0, 2.0 and 3.0 and a ray parameter of 0.06 s/km. H: crustal thickness; k: crustal average Vp/Vs ratio; Vpt and kt represent the true values of crustal P-wave velocity and average Vp/Vs ratio, respectively. SiS: i km single sediment layer; SiG: i km gradual sediment layer (multiple layers); CMZ: zip crust-mantle transition; CMG: gradual crust-mantle transition; SiCMZ: i km single sediment layer and zip crust-mantle transition; SiCMG: i km single sediment layer and gradual crust-mantle transition. s.Ps, s.PpPs, and s.PpSs + PsPs represent the phases from the bottom interface of the sedimentary layer.

negative and vary mainly by ± 10% and ± 5%, respectively. The H-k stacking in different Gaussian factors is shown for two typical stations (Fig. 10c): the station SCLINT is located in the Shaanxi-Shanxi Rift, and the other station SCHYS is located in the Sichuan Basin. For the station SCHYS (Fig. 10e), H increases and k decreases as the Gaussian factor increases. Clear phases associated with sediment exist between the direct P phase and Ps phase of the Moho. For different Gaussian factors, the PpPs phases of the Moho are clear and show good consistency. These observations show that the variations in H and k with different Gaussian factors may be mainly related to the overlying sediment and are not induced by the CMT. For the station SNLINT (Fig. 10f), H decreases as the Gaussian factor increases, and k increases as the Gaussian

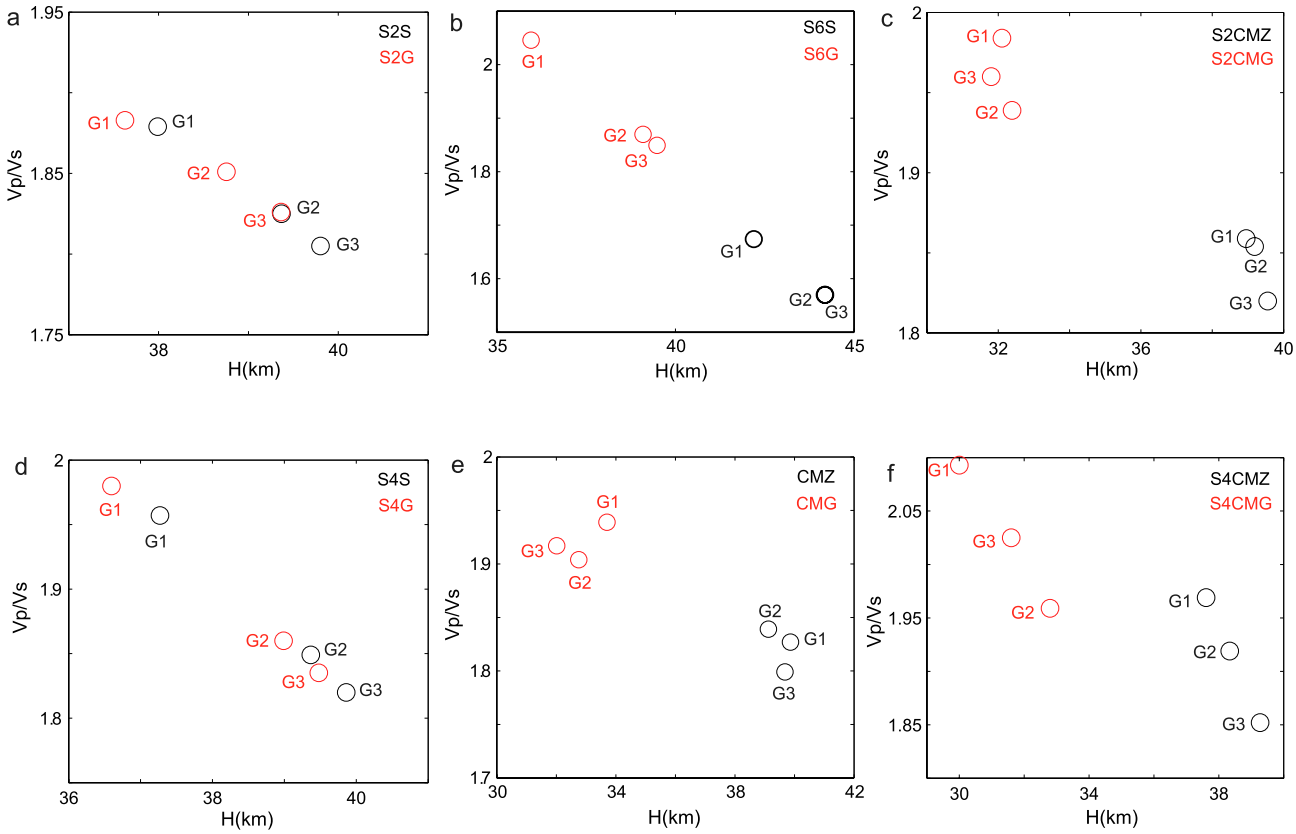

Fig. 9. The variations of H and Vp/Vs ratio with different Gaussian factors (Gi) of 1.0, 2.0 and 3.0 for synthetic H-k stacking results for different crustal models. SiS: i km single sediment layer; SiG: i km gradual sediment layer (multiple layers); CMZ: zip crust-mantle transition; CMG: gradual crust-mantle transition; SiCMZ: i km single sediment layer and zip crust-mantle transition; SiCMG: i km single sediment layer and gradual crust-mantle transition.

Table 1
The difference in synthetic H-k stacking results for different crustal models with Gaussian values (G) of 1.0, 2.0 and 3.0 and a ray parameter of 0.06 s/km. Hi: crustal thickness for a Gaussian factor of i; ki: crustal average Vp/Vs ratio for a Gaussian factor of i; Ht and kt represent the true crustal thickness and average Vp/Vs ratio, respectively. dH: (H-Ht)/H; dk: (k-kt)/k; SiS: i km single sediment layer; SiG: i km gradual sediment layer (multiple layers); CMZ: zip crust-mantle transition; CMG: gradual crust-mantle transition; SiCMZ: i km single sediment layer and zip crust-mantle transition; SiCMG: i km single sediment layer and gradual crust-mantle transition.

Models	dH(G = 1)	dk(G = 1)	dH(G = 2)	dk(G = 2)	dH(G = 3)	dk(G = 3)	(H3-H1)/H3	(k3-k1)/k3	(H3-H2)/H3	(k3-k2)/k3
S2S	−5.29%	4.68%	−1.61%	1.86%	−0.50%	0.78%	4.55%	−4.10%	1.09%	−1.11%
S4S	−7.32%	7.92%	−1.61%	2.54%	−0.35%	0.99%	6.50%	−7.53%	1.24%	−1.59%
S6S	5.21%	−8.30%	9.49%	−15.48%	9.46%	−15.48%	4.48%	−6.62%	0.03%	0
S2G	−6.31%	4.89%	−3.21%	3.24%	−1.62%	1.92%	4.41%	−3.12%	1.54%	−1.37%
S4G	−9.30%	8.99%	−2.59%	3.12%	−1.31%	1.80%	7.31%	−7.90%	1.24%	−1.36%
S6G	−11.23%	11.39%	−2.31%	3.05%	−1.30%	1.95%	8.92%	−10.65%	0.98%	−1.14%
CMZ	−0.34%	2.57%	−2.22%	3.21%	−0.81%	1.06%	−0.47%	−1.56%	1.38%	−2.22%
CMG	−18.68%	8.20%	−22.12%	6.51%	−24.94%	7.15%	−5.28%	−1.15%	−2.31%	0.68%
S2CMZ	−2.70%	3.66%	−2.07%	3.40%	−1.13%	1.59%	1.53%	−2.14%	0.92%	−1.87%
S4CMZ	−6.35%	8.48%	−4.32%	6.10%	−1.86%	2.70%	4.23%	−6.32%	2.36%	−3.62%
S2CMG	−24.58%	9.72%	−23.50%	7.63%	−25.76%	8.62%	−0.95%	−1.22%	−1.83%	1.07%
S4CMG	−33.33%	13.90%	−21.97%	8.01%	−26.58%	11.01%	5.07%	−3.36%	−3.78%	3.26%

factor increases. Clear phases associated with sediment appear between the direct P phase and Ps phase of the Moho. In addition, the PpPs phase of the Moho is disturbed by other phases to some degree. These observations show that the variations in H and k with different Gaussian factors may be related to both sediment and the CMT. The H-k stacking results for these two stations are consistent with previous observations demonstrating that thick sediment exists in the Sichuan Basin and that sediment and the intrusion of mantle material may be present in the Shaanxi-Shanxi Rift (Jiang et al., 2013; Wei et al., 2016; Wang et al., 2017). The above real observations and synthetic tests suggest that the sediment and CMT in most of the study region are not sharp and are not negligible for the detailed study of the deep structure. Although the structural influence between the bottom of the sediment and the top of the CMT is not considered in the theoretical analysis for H-k stacking, the synthetic tests for H-k stacking and waveforms with different frequencies can provide some information for the study of crustal structural by RF methods.

5.2. Crustal structural characteristics in different tectonic units

Similar and different crustal structures were observed in the different tectonic units (Fig. 6,7). The average S-wave velocity and thickness of the major layers in crust were further calculated to compare the structural differences in the Sichuan Basin, the Ordos Block,

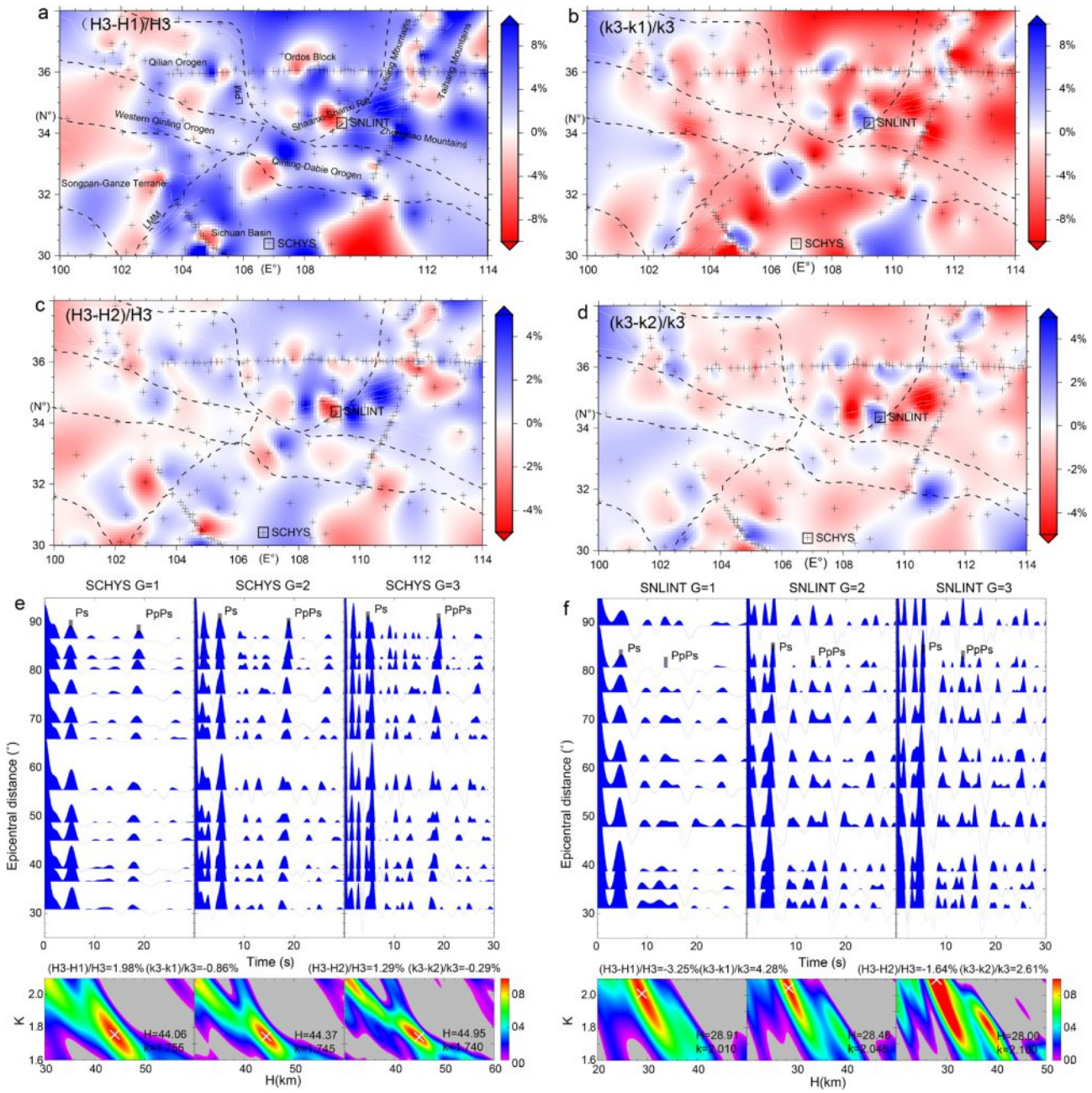

Fig. 10. The differences in H-k stacking with frequencies (a, b, c, d), waveforms and H-k stacking results for two typical stations (e, f) with different Gaussian factors (G) in the study region. In Hi and ki, i represents the Gaussian factor.

Table 2
The average S-wave velocity (Vs) and thickness (Th) in the upper crust (Upp.), the middle crust (Mid.) and the lower crust (Low.) in different tectonic units in the study region. SB: Sichuan Basin; OB: Ordos Block; TNCO: Trans-North China Orogen; QD: Qinling-Dabie Orogen; TP: Tibetan Plateau.

Parameters/Units	SB	OB	TNCO	QD	TP
Vs (Upp.) (km/s)	3.01	3.16	3.23	3.38	3.25
Th (Upp.) (km)	15.0	14.4	14.2	14.6	19.2
Vs (Mid.) (km/s)	3.70	3.70	3.68	3.67	3.64
Th (Mid.) (km)	11.0	17.0	17.1	16.9	27.0
Vs (Low.) (km/s)	3.96	3.99	3.95	3.99	4.01
Th (Low.) (km)	16.4	13.2	6.1	7.7	8.8

the Trans-North China Orogen, the Qinling-Dabie Orogen and the northeastern Tibetan Plateau (Table 2). Referring to the global seismic Vp of 6.4–6.8 km/s in the middle crust (Christensen and Mooney, 1995) and the global crustal average Vp/Vs ratio of 1.78 (Zandt and Ammon, 1995) and the inverted H (Fig. 6), we set < 3.60 km/s, 3.60–3.82 km/s and > 3.82 km/s to the Vs of the upper, middle and lower crust, respectively, to estimate the Vs and thickness of the layers for each station. Then, we calculated the average of the Vs and thickness from all stations in the different tectonic units referred to the classification of stations in Fig. 3b. In general, the average H thickens in the Trans-North China Orogen, the Qinling-Dabie Orogen, the Sichuan Basin, the Ordos Block and the northeastern Tibetan Plateau in turn. The average values of Vs in the upper crust and thickness in the lower crust in the Sichuan Basin and Ordos Block are significantly lower and thicker, respectively, than those in the Trans-North China Orogen, the Qinling-Dabie Orogen and the northeastern Tibetan Plateau. The average values of Vs and

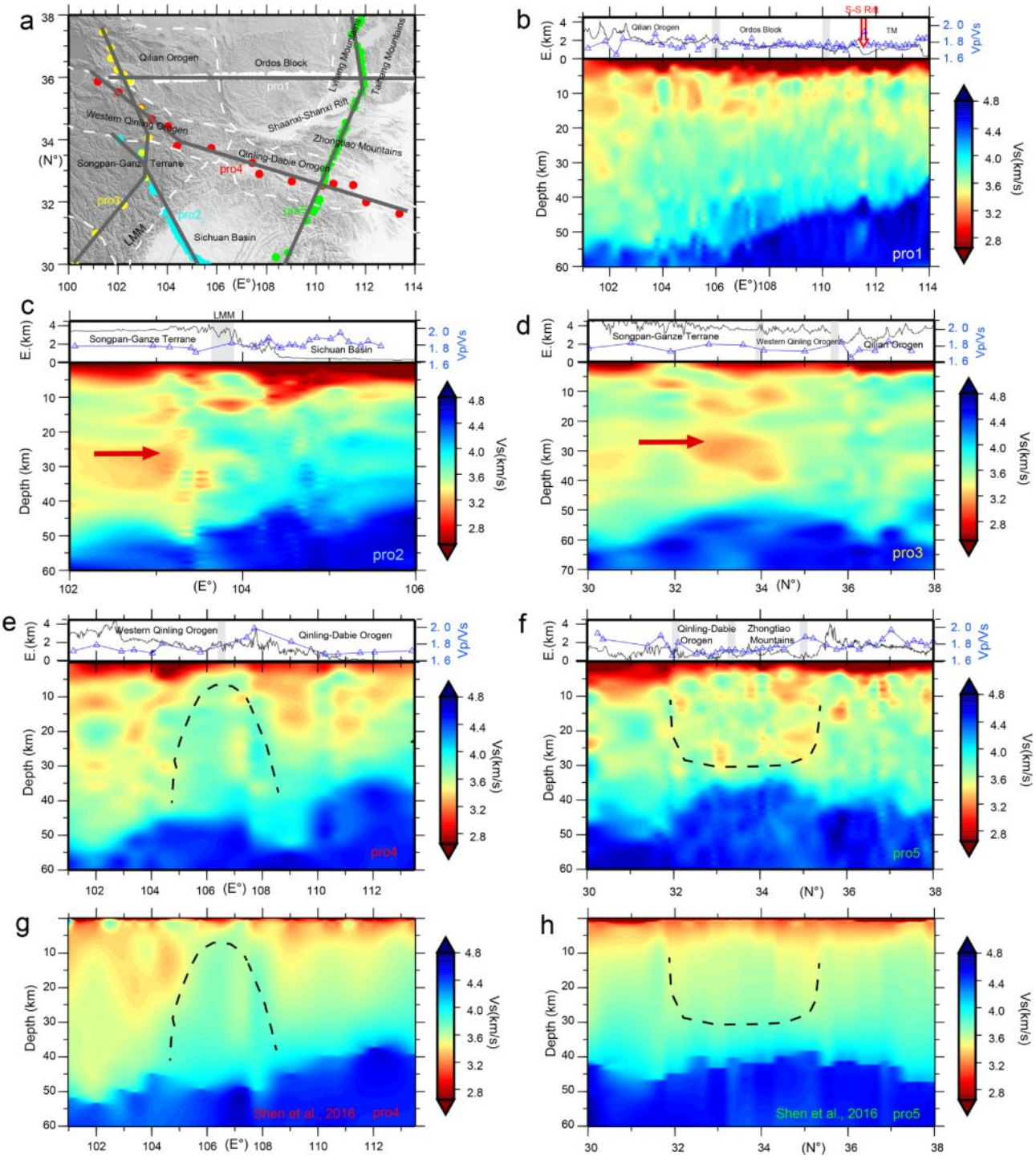

Fig. 11. S-wave velocity, Vp/Vs ratio and elevation (E.) beneath typical profiles (b,c,d,e,f) across different tectonic units. Grey lines (a) mark the location of the profiles. Red arrows (c,d) show the direction of the lower crustal flow. Dashed lines (e, g) outline the high S-wave velocity at the juncture region between the Western Qinling Orogen and the Qinling-Dabie Orogen both observed in this study and surface wave dispersion (Shen et al., 2016). Dashed lines (f, h) outline the different S-wave velocity beneath the Zhongtiao Mountains and adjacent Qinling-Dabie Orogen observed in this study and surface wave dispersion (Shen et al., 2016). LMM: Longmen Mountains; TM: Taihang Mountains; S-S Rift: Shaanxi-Shanxi Rift. (For interpretation of the references to color in this figure legend, the reader is referred to the web version of this article.)

thickness in the middle crust are lower and thicker, respectively, in the northeastern Tibetan Plateau than the other units (Table 2).

Striking differences in crustal structure were observed among different orogens with different formation ages and tectonic evolution histories. The phase velocity in different periods and the S-wave velocity at different depths in the Cenozoic northeastern Tibetan Plateau are obviously lower than those in the Qinling-Dabie Orogen, which formed in the Triassic (Fig. 3d and 7). In the Qinling-Dabie Orogen, H is approximately 50 km in the west and 35 km in the east, roughly bounded by 110°E, and this region exhibits significant lateral inhomogeneity in k and S-wave velocity. The E-W difference in H may be subjected to the compressional tectonic setting in the west and tensional tectonic setting in the east (Ren et al., 2002). In the northeastern Tibetan Plateau, H is generally > 45 km, and k is generally low and varies mainly from 1.7 to

1.8 (Fig. 6). Unlike the low-velocity anomaly present throughout the middle-lower crust in the Songpan-Ganze Terrane, similar anomalies only exist in local areas in the Western Qinling Orogen and Qilian Orogen (Figs. 7, 11). These observations, together with higher k values in the lower crust than in the upper crust (Christensen, 1996), suggest that crustal thickening may have mainly occurred in the upper crust in the Western Qinling Orogen and Qilian Orogen.

Similarities and differences in crustal structure were also imaged among different cratons. The phase velocity values are generally similar among the Ordos Block, the Sichuan Basin and the Trans-North China Orogen, although the phase velocities of $<$ 30 s are relatively lower in the Sichuan Basin and higher in the Trans-North China Orogen (Fig. 3c). Thick sediment and thick middle-lower crust with high S-wave velocity were imaged in the Ordos Block and the Sichuan Basin (Figs. 7, 11, Table 2). These observations, combined with the low resistance at the top and high resistance in the middle and lower crust (Zhang et al., 2012) and weak fossil anisotropy (Wang et al., 2014), suggest that the two regions retain ancient cratonic crust in their core. Similarly high S-wave velocities in the middle-lower crust were observed in the Longmen Mountains and adjacent Sichuan Basin (Fig. 11c), which supports the view that the rigid crust of the Sichuan Basin might have become wedged into the Tibetan crust in the Longmen Mountains (Wang et al., 2018).

Compared to the surroundings, the Zhongtiao Mountains of the Trans-North China Orogen and adjacent Qinling-Dabie Orogen to the south feature a thinner crust of $<$ 36 km and lower Vp/Vs ratios of $<$ 1.75 (Fig. 6). A low-velocity anomaly of $<$ 3.4 km/s was generally imaged in the middle-lower crust in this area (Fig. 11 f) but was not observed in the latest surface wave tomography (Shen et al., 2016, Fig. 11*h*). The theoretical RFs and phase velocity dispersion curves were further calculated assuming that the low-velocity anomaly did not exist. The results show obvious differences between the real data and theoretical RFs and curves, suggesting the reliability of the low-velocity anomaly. Geochemical observations (Gao et al., 1998) suggest that delamination of the lower crust occurred in the North China Craton and the Qinling-Dabie Orogen. A significant low-velocity anomaly was imaged in the upper mantle beneath the Trans-North China Orogen by body-wave and surface wave tomography (Jiang et al., 2013; Zhao et al., 2013). However, the low-velocity anomaly does not extend to the top of lithosphere mantle based on recent surface wave dispersion work (Jiang et al., 2013; Shen et al., 2016). The above observations show that the crust is probably unaffected by low-velocity material in the mantle in this area, which is consistent with the lower k in the crust (Fig. 6). The observed thin crust, low Vp/Vs ratio and low S-wave velocity anomaly suggest that delamination of the lower crust may have occurred in this area. Considering the tectonic evolution history in the area, we propose that the crust thickened in the collision between the North China Craton and the South China Block in the Triassic (Li et al.,1993; Ren et al., 2002) and that the lower crust delaminated during the extensional setting related to the westward subduction of the Pacific Plate beneath the Eurasian Plate since the Cenozoic (Ren et al., 2002; Zhao et al., 2005).

5.3. Crustal evolution and interaction in the study region

Obvious differences in the crustal structure were imaged among the northeastern Tibetan Plateau, the North China Craton, the South China Block and the Qinling-Dabie Orogen in our study. The cores of the Ordos Block and the Sichuan Basin retain the crustal structure of the ancient craton. The delamination of the lower crust likely occurred in the Zhongtiao Mountains of the Trans-North China Orogen and adjacent Qinling-Dabie Orogen to the south. Recently, the lower crustal ductile flow model has been widely used to explain the uplift process of the Tibetan Plateau (Clark and Royden, 2000). According to this model, the rheologically weaker Tibetan lower crust flows to the east in reaction to the continuous N-S India-Asia collision. At the eastern margin of the Tibetan Plateau, the crustal flow encounters the rigid Sichuan Basin and splits into two branches: one flows to southeast, and the other flows northeast along the Western Qinling. The two redirected branches create topography with a shallow gradient in the two areas and a steep gradient along the Longmen Mountains. The lower crustal flow model is supported by magnetotelluric observations (e.g., Bai et al., 2010) and GPS data (e.g., Gan et al., 2007) and is consistent with the widespread low-velocity anomaly in the middle-lower crust of the northeastern Tibetan Plateau evidenced by surface wave tomography (Zheng et al., 2010a, 2010b; Bao et al., 2013; Jiang et al., 2016). Shen et al. (2015) studied the lower velocity and azimuthal anisotropy simultaneously and speculated that the anisotropic low-velocity lower crust in the northeastern Tibetan Plateau is consistent with the lower crustal flow model. In this study, a widespread low-velocity anomaly was imaged in the middle-lower crust in the Songpan-Ganze Terrane (Figs. 7, 11), which supports the lower crust flow model. However, we only observed local and disconnected low-velocity anomalies beneath the Western Qinling Orogen and Qilian Orogen, which suggests that there is probably no lower crust flow in these two regions. In addition, at the juncture region between the Western Qinling Orogen and the Qinling-Dabie Orogen, the S-wave velocity is relatively higher in the middle-lower crust than in the adjacent eastern and western parts (Fig. 11e), which was also imaged by surface wave tomography (Shen et al., 2016; Fig. 11g). The above observations suggest that juncture region may have acted as a barrier impeding the inflow of lower crustal material into the Qinling-Dabie Orogen. Based on our observations and previous results, we propose that lower crustal flow encounters the rigid Sichuan Basin and splits into two branches: one flows to the southeast, and another flows northeast and is restricted to the central area in the Western Qinling Orogen. The crustal flow in the central Tibetan Plateau does not flow into the Qilian Orogen or the Qinling-Dabie Orogen (Fig. 12). Delamination of the lower crust may have occurred in the Zhongtiao Mountains of the Trans-North China Orogen and adjacent Qinling-Dabie Orogen to the south, which may be related to its formation history and extensional setting related to the westward subduction of the Pacific Plate since the Cenozoic.

6. Conclusions

We applied the multifrequency H-k stacking of RFs, RF nonlinear inversion, and joint inversion of RF and surface wave dispersion to image the Moho depth, k and crustal S-wave velocity at the juncture region of the northeastern Tibetan Plateau, the North China Craton, the South China Block and the Qinling-Dabie Orogen. The imaging results, together with the theoretical analysis of multifrequency H-k stacking, were further used to study the crustal structure and related tectonic evolution.

Our results show that H generally increases and k generally decreases as the Gaussian factor increases in the study region, which is consistent with the synthetic tests of H-k stacking of RFs. Typical cratonic crustal structures were observed in the core of the Ordos Block and the Sichuan Basin, while delamination of the lower crust may have occurred on the southern edge of the Trans-North China Orogen and adjacent Qinling-Dabie Orogen to the south. The lower crustal flow in the central Tibetan Plateau is probably restricted to the central area in the Western Qinling Orogen and does not flow into the Qilian Orogen or the Qinling-Dabie Orogen.

CRediT authorship contribution statement

Zigen Wei: Investigation, Writing - original draft, Software. **Zhiwei Li:** Conceptualization, Writing - review & editing. **Ling Chen:** Writing - review & editing, Resources. **Risheng Chu:** Writing - review & editing. **Shanshan Wu:** Data curation. **Yuan Ling:** Data curation. **Qiu Zeng:** Data curation.

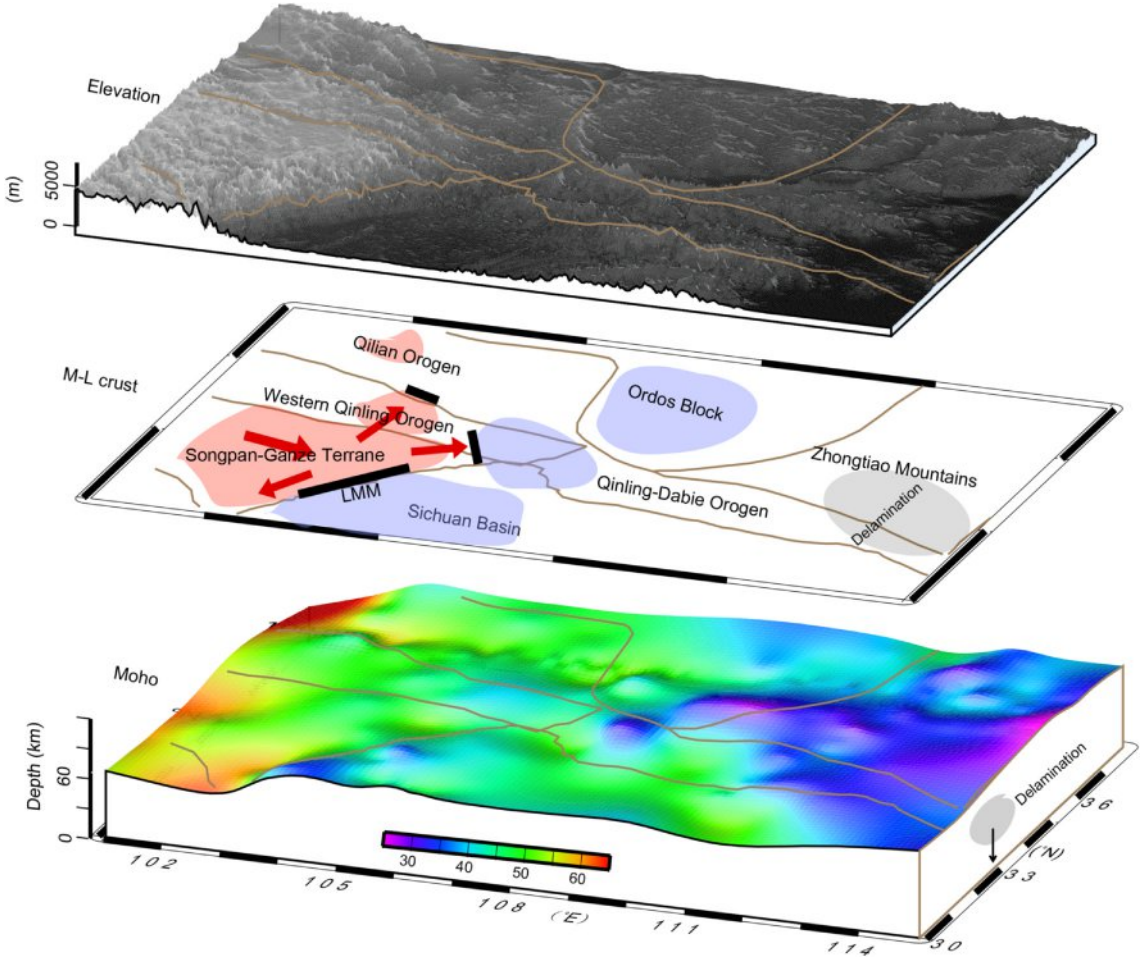

Fig. 12. Schematic diagram of elevation, Moho depth and lower crustal flow in the study region. Red and blue areas generally represent the low-velocity and high-velocity bodies, respectively. Red arrows indicate the lower crustal flow, and black bars represent barriers impeding the lower crustal flow. (For interpretation of the references to color in this figure legend, the reader is referred to the web version of this article.)

Declaration of Competing Interest

The authors declare that they have no known competing financial interests or personal relationships that could have appeared to influence the work reported in this paper.

Acknowledgments

The authors are grateful to the Seismic Array Laboratory, Institute of Geology and Geophysics, Chinese Academy of Sciences (doi:10.12129/IGGSL.Data.Observation) and Data Management Centre of China National Seismic Network at Institute of Geophysics (SEISDMC, doi:10.11998/SeisDmc/SN), China Earthquake Administration, for providing seismic data of temporary and permanent stations, respectively. We also thank Editor and two anonymous reviewers for their constructive reviews. This work is supported by the DREAM project of the National Key R&D Program of China (2016YFC0600402) and the State Key Laboratory of Marine Geology, Tongji University (No. MG201902) and the National Natural Science Foundation of China (Grants 41604056).

Appendix A. Supplementary material

Supplementary data to this article can be found online at https://doi.org/10.1016/j.jseaes.2020.104535.

References

Bai, D.H., Unsworth, M.J., Meju, M.A., Ma, X.B., Teng, J.W., Kon, X.R., Sun, Y., Sun, J., Wang, L.F., Jiang, C.S., Zhao, C.P., Xiao, P.F., Liu, M., 2010. Crustal deformation of the eastern Tibetan plateau revealed by magnetotelluric imaging. NatureGeoscience 3 (5), 358–362.

Bao, X.W., Song, X.D., Xu, M.J., Wang, L.S., Sun, X.X., Mi, N., Yu, D.Y., Li, H., 2013. Crust and upper mantle structure of the North China Craton and the NE Tibetan Plateau and its tectonic implications. Earth Planet Sci Lett 369 (370), 129–137.

Chen, L., Cheng, C., Wei, Z.G., 2009. Seismic evidence for significant lateral variations in lithospheric thickness beneath the central and western North China Craton. Earth Planet. Sci. Lett. 286, 171–183.

Christensen, N.I., 1996. Poisson's ratio and crustal seismology. J. Geophys. Res. 101, 3139–3156.

Christensen, N.I., Mooney, W.D., 1995. Seismic velocity structure and composition of the continental crust: a global view. J. Geophys. Res. 100, 9761–9788.

Clark, M.K., Royden, L.H., 2000. Topographic ooze, Building the eastern margin of Tibet by lower crustal flow. Geology 28 (8), 703–706.

Deng, Q.D., Zhang, P.Z., Ran, Y.K., Yang, X.P., Min, W., Chu, Q.Z., 2003. Basic characteristics of active tectonics of China. Science in China (Series D) 46 (4), 356–372.

Deng, Y.F., Li, J.T., Song, X.D., Zhu, L.P., 2018. Joint inversion for lithospheric structures, Implications for the growth and deformation in northeastern Tibetan Plateau. Geophys. Res. Lett. 45, 3951–3958.

Gan, W.J., Zhang, P.Z., Shen, Z.K., Niu, Z.J., Wang, M., Wang, Y.G., Zhou, D.M., Cheng, J., 2007. Present-day crustal motion within the Tibetan Plateau inferred from GPS measurements. J. Geophys. Res. 112, B08416. https://doi.org/10.1029/2005JB004120.

Gao, S., Luo, T.C., Zhang, B.R., Zhang, H.F., Han, Y.W., Zhao, Z.D., Hu, Y.K., 1998. Chemical composition of the continental crust as revealed by studies in East China. Geochimica Cosmochimca Acta 62, 1959–1975.

Griffin, W.L., Zhang, A.D., O'Reilly, S.Y., Ryan, C.G., 1998. Phanerozoic evolution of the lithosphere beneath the Sino-Korean Craton. In, Flower, M., Chung, S.L., Lo, C.H., Lee, T.Y. (Eds.), Mantle Dynamics and Plate Interactions in East Asia, American Geophysics Union Geodynamics Series 27, 107-126.

He, R.Z., Shang, X.F., Yu, C.Q., Zhang, H.J., Van der Hilst, R., 2014. A unified map of Moho depth and Vp/Vs ratio of continental China by receiver function analysis. Geophys. J. Int. 199, 1910–1918.
Herrmann, R.B., 2013. Computer programs in seismology, An evolving tool for instruction and research. Seism Res Lett. 84 (6), 1081–1088.
Hu, J.F., Zhu, X.G., Xia, J.Y., Chen, Y., 2005. Using Surface Wave and Receiver Function to Jointly Inverse the Crust-Mantle Velocity Structure in the West Yunnan Area. Chin. J. Geophys. 48 (5), 1148–1155 (in Chinese).
Ji, S.C., Wang, Q., Salisbury, M.H., 2009. Composition and tectonic evolution of the Chinese continental crust constrained by Poisson's ratio. Tectonophysics 463, 15–30.
Jiang, C.X., Yang, Y.J., Zheng, Y., 2016. Crustal structure in the junction of Qinling Orogen, Yangtze Craton and Tibetan Plateau, implications for the formation of the Dabashan Orocline and the growth of Tibetan Plateau. Geophys. J. Int. 205 (3), 1670–1681.
Jiang, M.M., Ai, Y.S., Chen, L., Yang, Y.J., 2013. Local modification of the lithosphere beneath the central and western North China Craton, 3-D constraints from Rayleigh wave tomography. Gondwana Res. 24 (3), 849–864.
Julià, J., Ammon, C.J., Herrmann, R.B., Correig, A.M., 2000. Joint inversion of receiver function and surface wave dispersion observations. Geophys. J. R. Astron. Soc. 143 (1), 99–112.
Laske, G., Masters, G., Ma, Z., 2013. Update on CRUST1.0 - A 1-degree Global Model of Earth's Crust[C]// EGU General Assembly Conference[C]. EGU General Assembly Conference Abstracts.
Levin, V., Park, J., 1997. Crustal anisotropy in the Ural Mountains foredeep from teleseismic receiver functions. Geophys. Res. Lett. 24, 1283–1286.
Li, S.G., Xiao, Y.L., Liou, D.L., Chen, Y.Z., Ge, N.J., Zhang, Z.Q., Sun, S.S., Cong, B.L., Zhang, R.Y., Hart, S.R., Wang, S.S., 1993. Collision of the North China and Yangtze Blocks and formation of coesite-bearing eclogites, timing and processes. Chem. Geol. 109, 89–111.
Li, S.L., Mooney, W.D., Fan, J.C., 2006. Crustal structure of mainland China from deep seismic sounding data. Tectonophysics 420, 239–252.
Li, X.H., Li, W.X., Li, Z.X., Lo, C.H., Wang, J., Ye, M.F., Yang, Y.H., 2009. Amalgamation between the Yangtze and Cathaysia Blocks in South China, Constraints from SHRIMP U-Pb zircon ages, geochemistry and Nd-Hf isotopes of the Shuangxiwu volcanic rocks. Precambr. Res. 174, 117–128.
Li, X.L., Li, Z.W., Hao, T.Y., Wang, S., Xing, J., 2017. A multi-frequency receiver function inversion approach for crustal velocity structure. Comput. Geosci 102(C),45–55.
Li, Z.W., Ni, S.D., Roecker, S., 2014. Interstation Pg and Sg differential traveltime tomography in the northeastern margin of the Tibetan plateau, Implications for spatial extent of crustal flow and segmentation of the Longmenshan fault zone. Phys. Earth Planet. Inter. 227, 30–40.
Ling, Y., Chen, L., Wei, Z.G., Jiang, M.M., Wang, X., 2017. Crustal S-velocity structure and radial anisotropy beneath the southern part of central and western North China Craton and the adjacent Qilian Orogenic Belt from ambient noise tomography. Science China Earth Sciences 60 (10), 1752–1768.
Liu, Q. Y., Van, Der Hilst. R. D., Li, Y., Yao, H. J., Chen, J. H., Guo, B., Qi, S. H., Wang, J., Huang, H., Li, S. C., 2014. Eastward expansion of the Tibetan Plateau by crustal flow and strain partitioning across faults. Nature Geoscience 7(5), 361-365.
Pan, S.Z., Niu, F.L., 2011. Large contrasts in crustal structure and composition between the Ordos plateau and the NE Tibetan plateau from receiver function analysis. Earth Planet. Sci. Lett. 303, 291–298.
Ren, J.Y., Tamaki, K., Li, S.T., Zhang, J.X., 2002. Late Mesozoic and Cenozoic rifting and its dynamic setting in Eastern China and adjacent areas. Tectonophysics 344, 175–205.
Shen, W.S., Ritzwoller, M.H., Kang, D., Kim, Y.H., Lin, F.C., Ning, J.Y., Wang, W.T., Zheng, Y., Zhou, L.Q., 2016. A seismic reference model for the crust and uppermost mantle beneath China from surface wave dispersion. Geophys. J. Int. 206 (2), 954–979.
Shen, X.Z., Yuan, X.H., Ren, J.S., 2015. Anisotropic low-velocity lower crust beneath the northeastern margin of Tibetan Plateau, Evidence for crustal channel flow. Geochemistry 16 (12). https://doi.org/10.1002/2015GC005952.
Tapponnier, P., 2001. Oblique Stepwise Rise and Growth of the Tibet Plateau. Science 294 (5547), 1671–1677.
Tian, X.B., Zhang, Z.J., 2013. Bulk crustal properties in NE Tibet and their implications for deformation model. Gondwana Res. 24 (2), 548–559.
Wang, C.Y., Sandvol, E., Zhu, L.P., Lou, H., Yao, Z.X., Luo, X.H., 2014. Lateral variation of crustal structure in the Ordos block and surrounding regions, North China, and its tectonic implications. Earth Planet. Sci. Lett. 387, 198–211.
Wang, X., Cheng, L., Ai, Y.S., Xu, T., Jiang, M.M., Ling, Y., Gao, Y.F., 2018. Crustal structure and deformation beneath eastern and northeastern Tibet revealed by P-wave receiver functions. Earth Planet. Sci. Lett. 497, 69–79.
Wang, W.L., Wu, J.P., Fang, L.H., Lai, G.J., Cai, Y., 2017. Sedimentary and crustal thicknesses and Poisson's ratios for the NE Tibetan Plateau and its adjacent regions based on dense seismic arrays. Earth Planet. Sci. Lett. 462, 76–85.
Wei, Z.G., Chen, L., Jiang, M.M., Ling, Y., 2015. Lithospheric structure beneath the central and western North China Craton and the adjacent Qilian orogenic belt from Rayleigh wave dispersion analysis. Tectonophysics 646, 130–140.
Wei, Z.G., Chen, L., Li, Z.W., Ling, Y., Li, J., 2016. Regional variation in Moho depth and Poisson' s ratio beneath eastern China and its tectonic implications. J. Asian Earth Sci. 115, 308–320.
Yan, D.P., Zhou, Y., Qiu, L., Wells, M.L., Mu, H., Xu, C.G., 2018. The Longmenshan tectonic complex and adjacent tectonic units in the eastern margin of the Tibetan Plateau: a review. J. Asian Earth Sci. 164, 33–57.
Ye, Z., Li, J., Gao, R., Song, X. D., Li, Q. S., Li, Y. K., Xu, X., Huang, X. F,, Xiong, X.S., Li, W. H., 2017. Crustal and uppermost mantle structure across the Tibet-Qinling transition zone in NE Tibet, Implications for material extrusion beneath the Tibetan Plateau. Geophysical Research Letters 10.1002/2017GL075141.
Yin, A., Harrison, T.M., 2000. Geologic evolution of the Himalayan-Tibetan orogen. Annu. Rev. Earth Planet. Sci. 28, 211–280.
Zandt, G., Ammon, C.J., 1995. Continental crust composition constrained by measurements of crustal Poisson' s ratio. Nature 374, 152–154.
Zhang, L.T., Jin, S., Wei, W.B., Ye, G.F., Duan, S.X., Dong, H., Zhang, F., Xie, C.L., 2012. Electrical structure of crust and upper mantle beneath the eastern margin of the Tibetan plateau and the Sichuan basin. Chin. J. Geophys. 55 (12), 4126–4137 (in Chinese).
Zhang, X.K., Li, S.L., Wang, F.Y., Jia, S.X., Fang, S.M., 2003. Differences of crustal structure between northeastern margin of Tibetan Plateau, the Ordos block, and Tangshan earthquake region in North China: Results of deep seismic sounding. Seismol. Geol. 25 (1), 52–60 (in Chinese).
Zhao, G.C., Sun, M., Wilde, S.A., Li, S.Z., 2005. Late Archean to Paleoproterozoic evolution of the North China Craton, key issues revisited. Precambr. Res. 136, 177–202.
Zhao, L., Zheng, T.Y., Lv, G., 2013. Distinct upper mantle deformation of cratons in response to subduction, Constraints from SKS wave splitting measurements in eastern China. Gondwana Res. 23, 39–53.
Zheng, T.Y., Zhao, L., Zhu, R.X., 2009. New evidence from seismic imaging for subduction during assembly of the North China Craton. Geology 37 (5), 395–398.
Zheng, X.F., Yao, Z.X., Liang, J.H., Zheng, J., 2010a. The role played and opportunities provided by IGP DMC of China National Seismic Network in Wenchuan earthquake disaster relief and researches. Bull. Seismol. Soc. Am. 100 (5B), 2866–2872. https://doi.org/10.1785/0120090257.
Zheng, Y., Yang, Y.J., Michael, Ritzwoller, 2010b. Crustal structure of the northeastern Tibetan plateau, the Ordos block and the Sichuan basin from ambient noise tomography. Earthq. Sci. 23 (5), 465–476.
Zhu, L.P., Kanamori, H., 2000. Moho depth variation in southern California from teleseismic receiver functions. J. Geophys. Res. 105, 2969–2980.